Electronic Supplementary Material (ESI) for Nanoscale.


***SUPPLEMENTAL MATERIALS***

# The Impact of Spatially Heterogeneous Chemical Doping on the Electronic Properties of CdSe Quantum Dots: Insights from ab initio Computation

*Priyanka Deswal,[a] Kushal Samanta,[b] Dibyajyoti Ghosh[b,c]**

[a] *Department of Physics, Indian Institute of Technology, Delhi, Hauz Khas, New Delhi 110016, India*

[b] *Department of Materials Science and Engineering, Indian Institute of Technology, Delhi, Hauz Khas, New Delhi 110016, India*

[c] *Department of Chemistry, Indian Institute of Technology, Delhi, Hauz Khas, New Delhi 110016, India*

* Corresponding authors; E-mails: dibyajyoti@iitd.ac.in

## S1. Structure of Bare Pristine and Doped QDs

The quantum dot consists of three distinct regions characterized by their atomic coordination, shown in Figure S1. The core region, consisting of 12 atoms, demonstrates bulk-type coordination with four bonds. The sub-surface region comprises 12 atoms within the QD and is bonded with four atoms. The surface region encompasses 42 atoms and comprises outer atoms bonded with three atoms. The surface and subsurface regions are distinguished based on the coordination of Cd/Cu atoms with the Se atom.[1] Previous research has indicated that surface atoms in QDs have lower coordination than core atoms.[1,2] These regions are subsequently substituted with copper (Cu) atoms to investigate the influence of Cu doping. The smaller ionic size of Cu (radii 73 pm) compared to Cd (97 pm) results in shorter Cu-Se bond lengths than their respective Cd-Se counterparts, leading to local compressive strain around the doped Cu atom shown in Figure S2. The surface Cu-Se bonds, with lower coordination numbers and higher degrees of freedom, exhibit greater contraction, introducing higher chemical pressure than the core- and sub-QD regions.

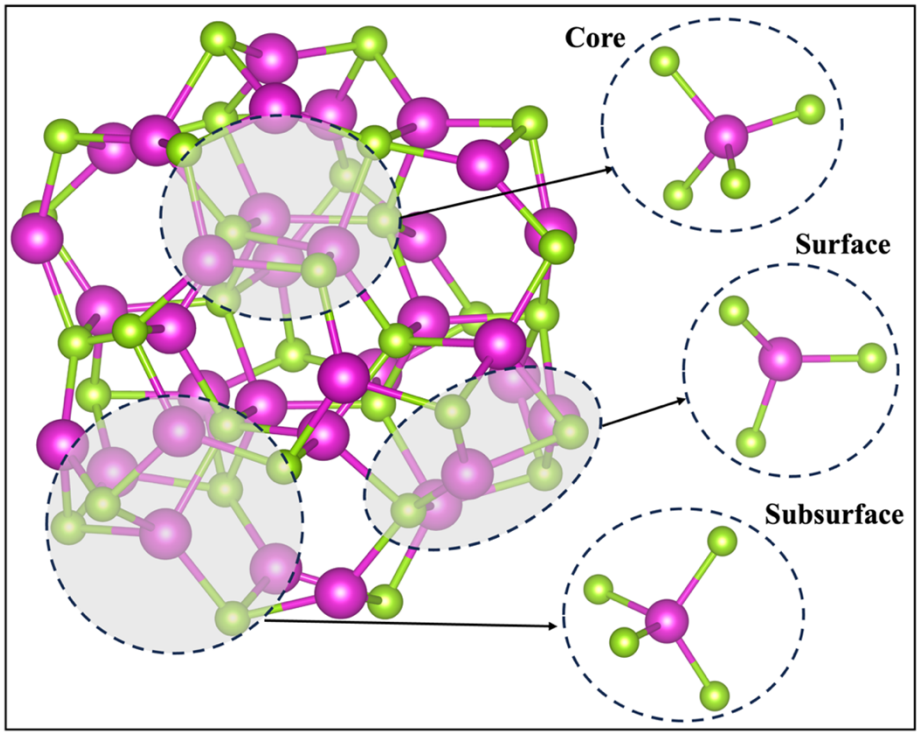

**Figure S1.** Schematic representation of a pristine $Cd_{33}Se_{33}$ quantum dot, illustrating the arrangement of atoms in the core, subsurface, and surface regions. The inset showcases a zoomed image of the coordination of atoms in the core, subsurface, and surface, highlighting three distinct regions of the quantum dot.

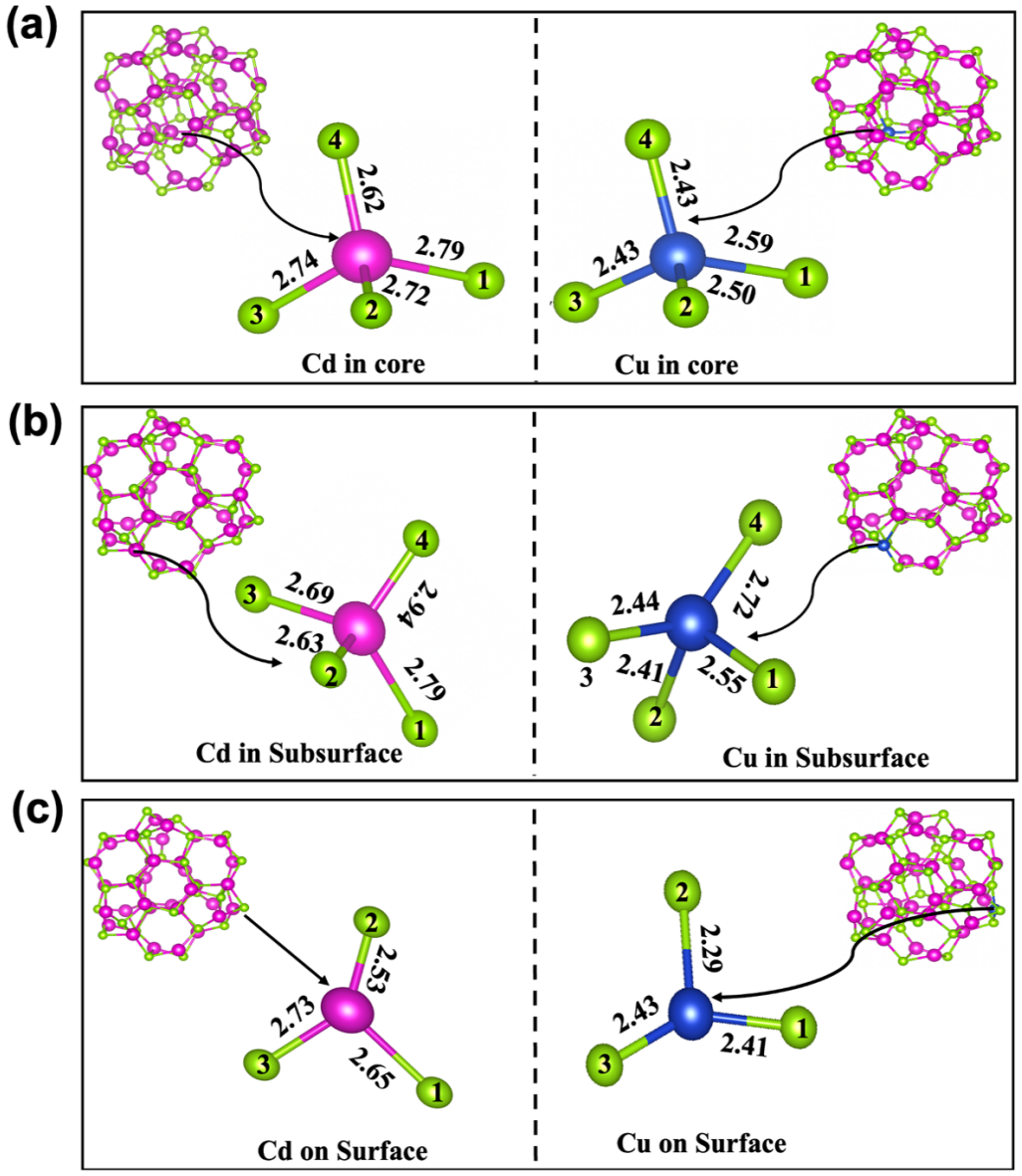


**Figure S2.** Comparison of Cu-Se bond length relative to their respective Cd-Se bonds in different regions of the quantum dot: (a) core-QD, (b) sub-QD, and (c) surf-QD.

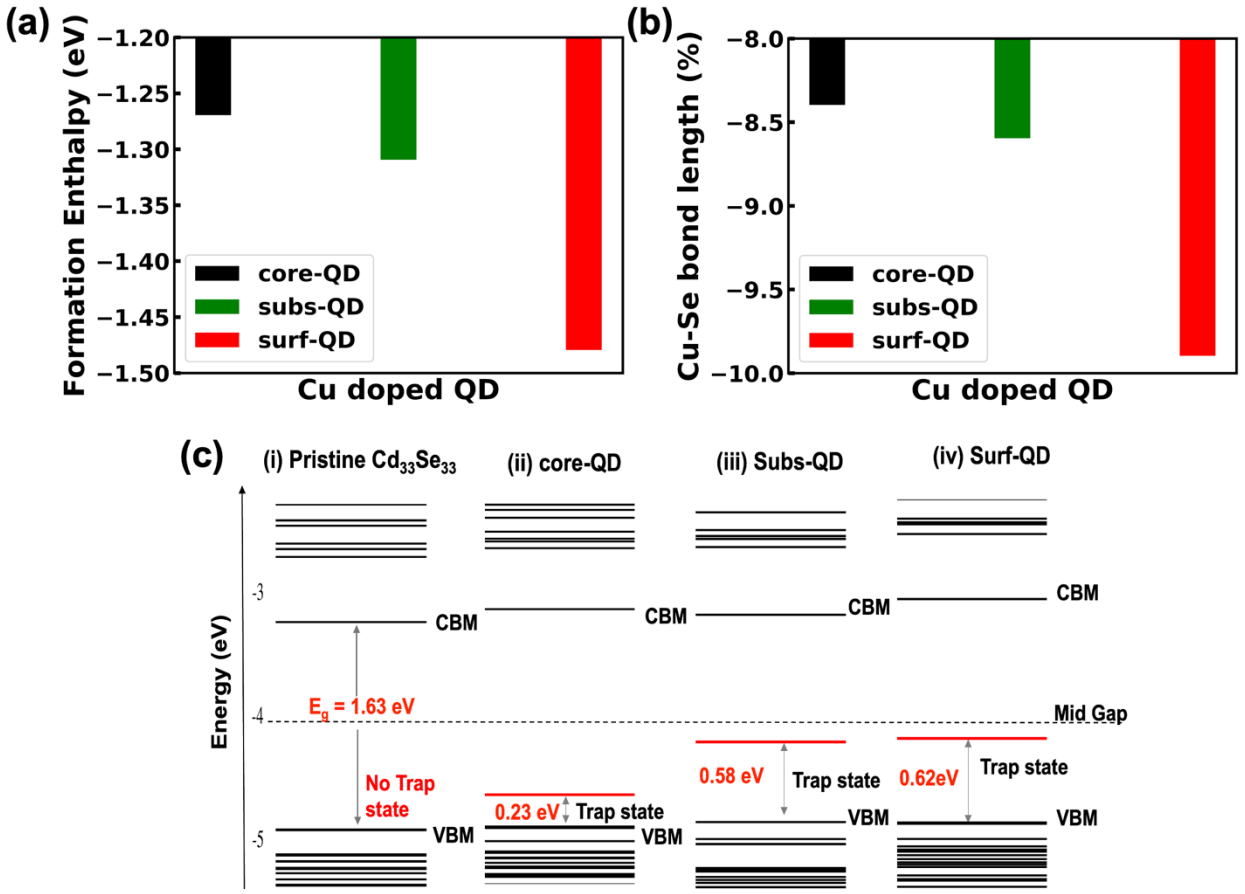


**Figure S3.** (a) Formation enthalpy ($H_{form}$) of the core-QD, subs-QD, and surf-QD (equation given in Section S5). (b) Percentage compression of average Cu-Se bond lengths compared to equivalent Cd-Se bonds of pristine $Cd_{33}Se_{33}$ as reference for core-QD, subs-QD, and surf-QD and (c) the simplified band diagram of the energy levels of pristine and doped QDs.

## S2. The positional distribution of Cu dopant on the surface

The low symmetry of the $Cd_{33}Se_{33}$ surface gives rise to various inequivalent sites for Cu doping. We have considered a few randomly selected QDs where the Cu atom is doped in different inequivalent surface positions to address this. As shown in Figure S4a,b the total relative potential energy varies marginally depending on the Cu position on the CdSe surface. However, we do not find a significant energetic preference for Cu atom occupying any particular surface site(s). The

total density of states (TDOS) also depicts minor changes in the overall electronic properties of Cu-doped QDs with different Cu positions shown in Figure S4c. Thus, variation in the Cu dopant position on the surface does not substantially influence the general energetics and electronic structure of these doped CdSe QDs.

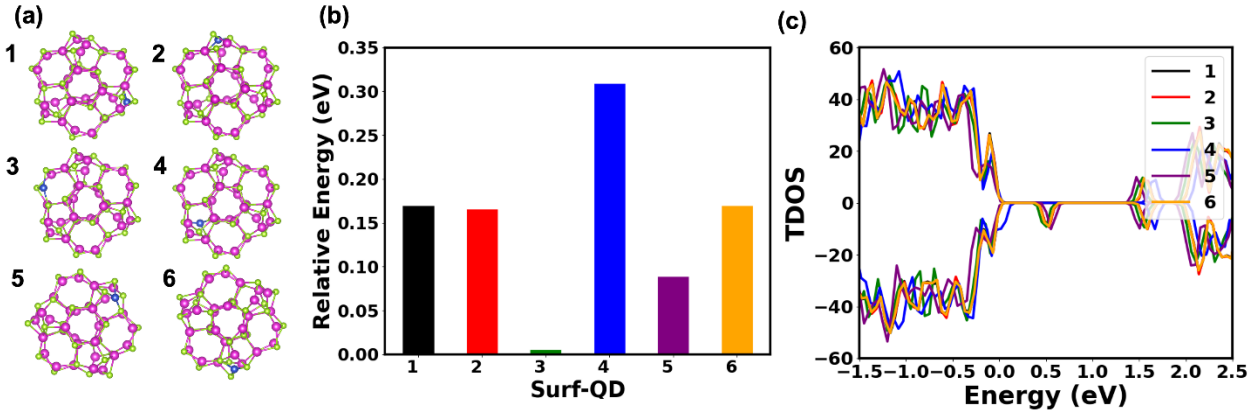


Figure S4: (a) Structures, (b) Bar graph illustrating relative total energy (with the most stable configuration as the reference(zero)), and (c) Total density of state (TDOS) showing the positional distribution of Cu dopant on the surface and their impact on the electronic properties.

**S3. The oxidation state of Cu**

We optimize the ground state of doped CdSe at different spin and charge states to understand the comparative stability of Cu in these QDs. The $3d^9$ and $3d^{10}$ configurations indicate the +2 and +1 oxidation states of Cu, respectively. The Cu $3d^9$ with a total spin moment of 1 $\mu_B$ is energetically more stable by 0.1-0.8 eV for core and surf-QDs with or without ligand ($NH_2Me$) passivation. Note that, the unpaired spin state in the minority channel appears as the mid-gap state in the pDOS plot shown in Figure 1f-h and TDOS plot in Figure S5a. The spin density plots in Figure S5b depict that the spin moment is dominantly localized at and near the Cu dopant site, highlighting its 3d9 configuration.

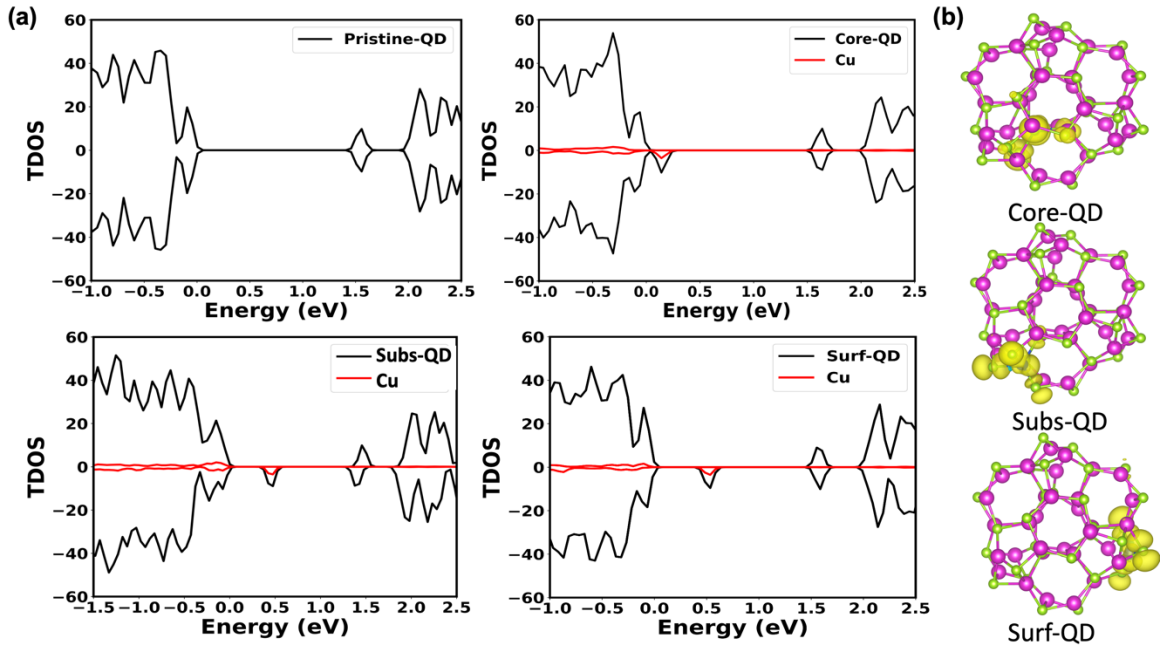


Figure S5: Total density of state (TDOS) and contribution of Cu in the density of state plot for bare QDs (a) pristine-QD, core-QD, subsurface-QD and surface-QD, (b) Spin density distributions for core-QD, subsurface-QD, and surface-QD. The spin density predominantly localizes on the Cu dopant atom irrespective of its position on the QD.

## S4. Structure and Electronic Properties of Ligand Passivated Pristine and Doped QDs

The construction of nearly spherical QDs by cleaving the bulk semiconductor lattice generates dangling bonds that can appear as mid-gap states inside the band gap.[4,5] To mitigate the presence of these dangling bonds and structurally stabilize these QDs, ligands passivate their surface. To explore the impact of ligand passivation on these Cu-doped CdSe QDs, we model the CdSe QDs passivated with several commonly used molecular ligands, methylamine ($NH_2Me$, Me is $CH_3$), methyl phosphine ($PH_2Me$), and trimethyl phosphine oxide ($POMe_3$) to passivate their surface.[1] As the ligands donate two electrons (L-type), the Cd-sites are considered the preferred site for surface-ligand binding.[6] Following previous reports, we passivated only nine two-coordinated surface Cd atoms before geometry optimization.[7] For each ligand, we consider three passivated

QD structures: (1) core-QD (core-QD-L), (2) surf-QD with unpassivated Cu-site (surf-QD-L), and (3) surf-QD with passivated Cu (surf-QD-$L_{Cu}$) and their structure and electronic properties are shown in Table S1 and Figure S6-S10. The structural relaxation depicts the marginal changes in the bond distances and angles in CdSe QDs with and without ligand passivation for all types of QDs considered here. Thus, ligand passivation insignificantly impacts the overall geometry of these stoichiometric QDs shown in Figure S6.

Like bare CdSe, the formation enthalpies in Figure S7 show that Cu doping is always energetically favorable irrespective of ligand type. Furthermore, the surf-QD-L has higher negative formation enthalpies than surf-QD-$L_{Cu}$ by 0.27-0.48 eV (Table S1). Such energetic order indicates a higher probability of realizing the unpassivated Cu site on the QD-L surfaces, like bare QDs. Thus, the presence of ligands would not drastically impact the local geometry of Cu on the surface. The plotted partial density of states in Figure S8a-d shows that the ligand passivation does not substantially impact the electronic properties of doped-CdSe. The midgap state in the minority spin channel above the VBM level remains unaltered primarily regarding energetic position with ligand passivation. Compared to bare QDs, the energy shifts for the mid-gap state in core-QD-L and surf-QD-L are |0.04| eV and |0.01| eV, respectively. The overall charge density (on the right panel of S7a-d) distributions in the VBM, CBM, and spin-polarized mid-gap state remain mostly unchanged for bare and passivated QDs. We do not find any contribution from the ligand orbitals in the trap state or near the band edges. These simulations emphasize that the surface ligand passivation does not impact the overall electronic characteristics, including the charge state of the dopant in $Cd_{32}Se_{33}Cu$ QDs. Overall, the electronic states of Cu-QDs remain mostly unaltered irrespective of the presence or absence of a passivating agent and the type of the passivating agent utilized (Figure S8-S10). Thus, the comprehensive analysis reveals that the surface passivating

molecular ligands exhibit marginal influences on the structural and electronic properties as compared to their bare counterpart. The high structural stability of these dangling bond-free magic-sized CdSe QDs primarily prevents ligand-induced surface reconstructions. Due to this, their robust electronic properties remain mostly unaltered in the presence of L-type ligands. Thus, we continue molecular dynamics simulations considering the bare QDs.

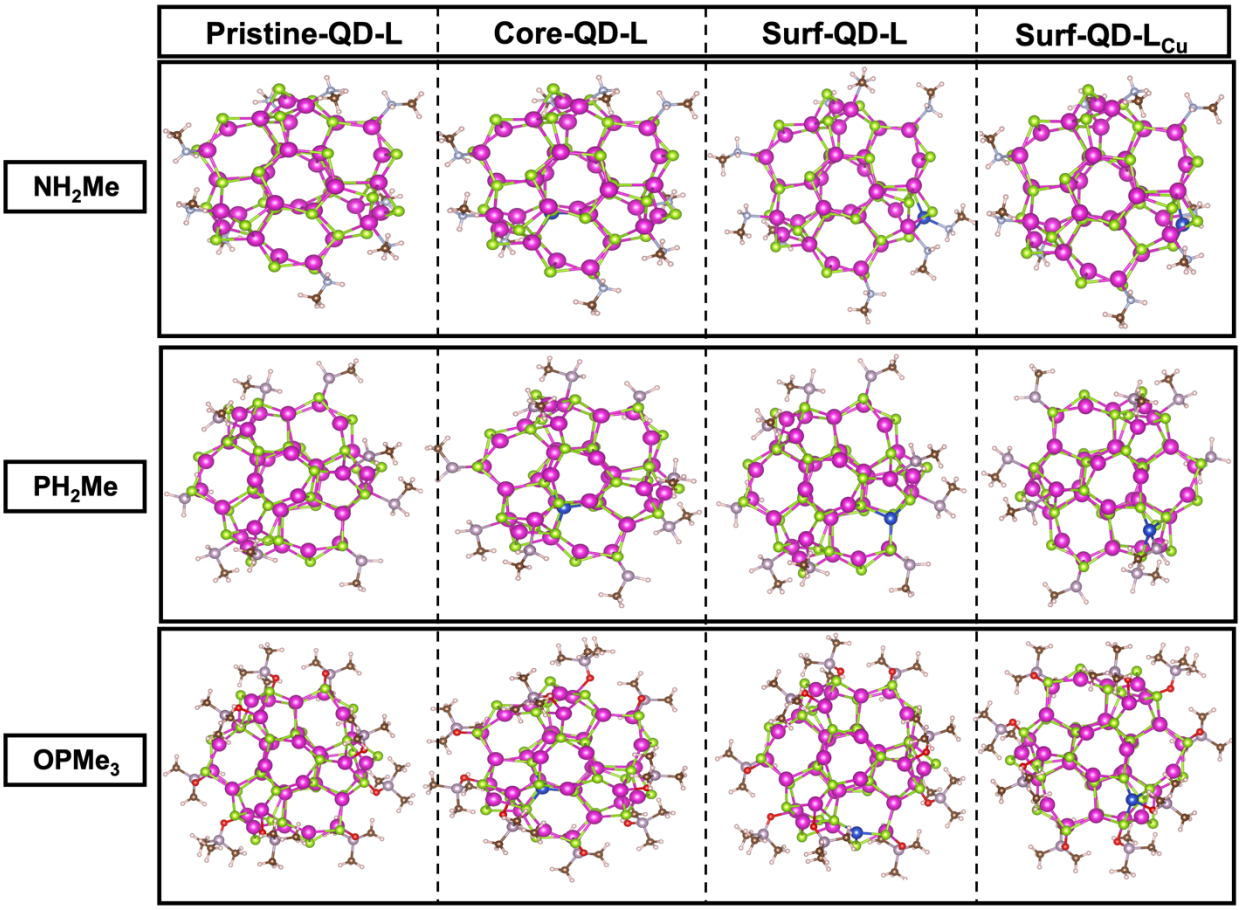


Figure S6: Structures of Pristine-QD-L (Pristine QD with L=ligand), core-QD (core-QD-L), surf-QD with unpassivated Cu-site (surf-QD-L), and surf-QD with passivated Cu (surf-QD-$L_{Cu}$) for L=$NH_2Me$, $PH_2Me$ and $OPMe_3$.

**Table S1**. The structural and electronic properties of $NH_2Me$ passivated core, sub, and surf-QDs.

| | Average bond length Cu-Se (Å) | Formation enthalpy (eV) | Defect state position (Above VBM) (eV) | Elemental Contribution in defect state (%) | | | Bader charge on Cu ($e^-$) |
|---|---|---|---|---|---|---|---|
| | | | | Se | Cu | Cd | |
| Core-QD-L | 2.49 | -1.29 | 0.27 | 49 | 33 | 18 | +0.46 |
| Surf-QD-L | 2.38 | -1.48 | 0.61 | 48 | 36 | 16 | +0.45 |
| Surf-QD-$L_{Cu}$ | 2.45 | -1.21 | 0.81 | 44 | 39 | 17 | +0.52 |

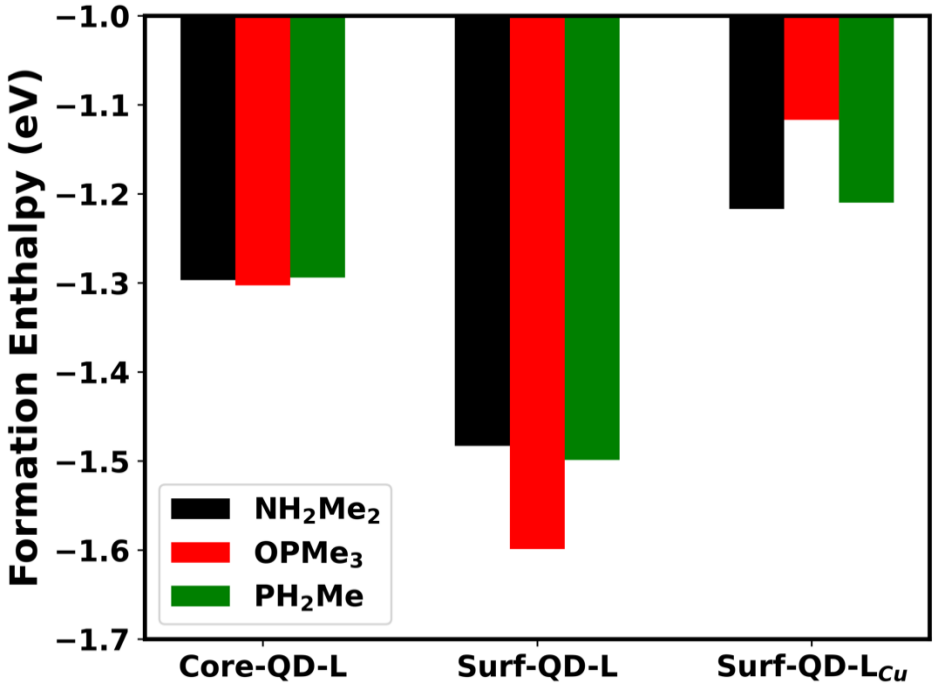


**Figure S7.** Formation enthalpy ($H_{form}$) of the core-QD, subs-QD, and surf-QD (equation given in Section S5).

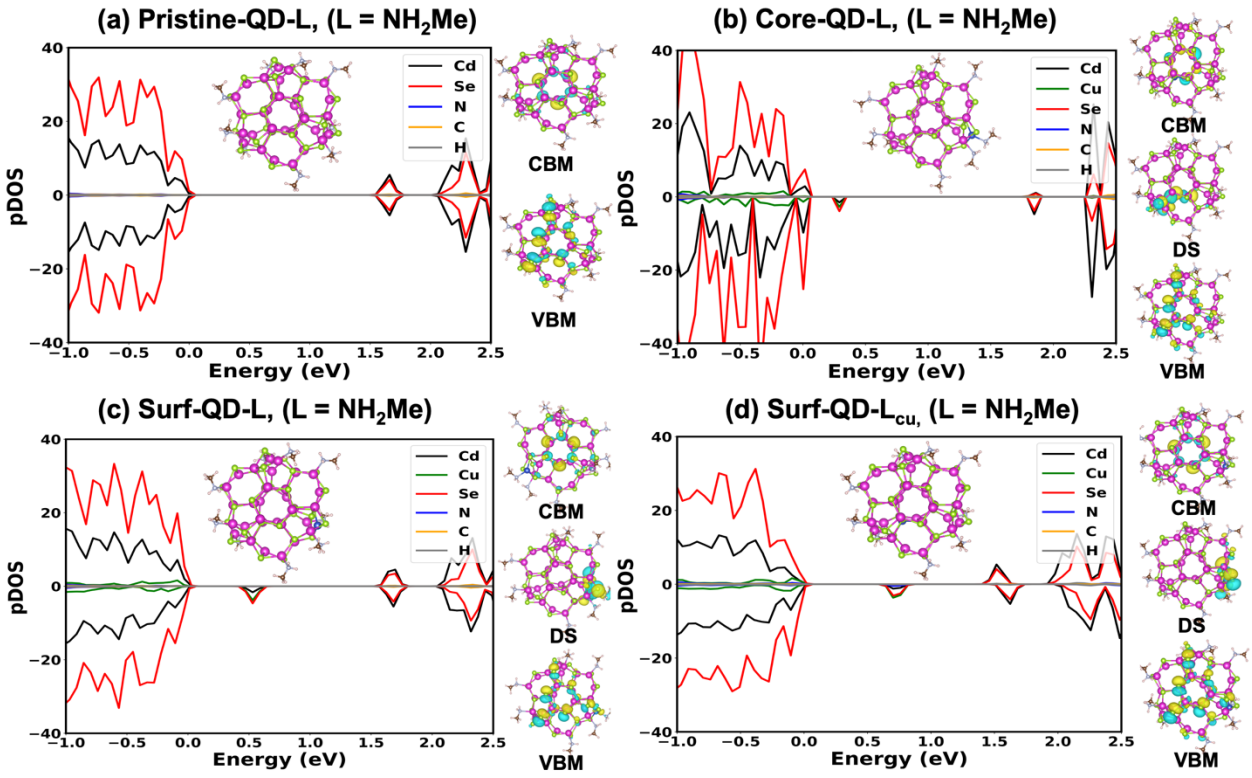


Figure S8: Optimized structures (in inset), the partial density of states (pDOS) and charge density (on the right panel) of (a) core-QD (core-QD-L), (b) surf-QD with unpassivated Cu-site (surf-QD-L), and (c) surf-QD with passivated Cu (surf-QD-$L_{Cu}$) where L=$NH_2Me$.

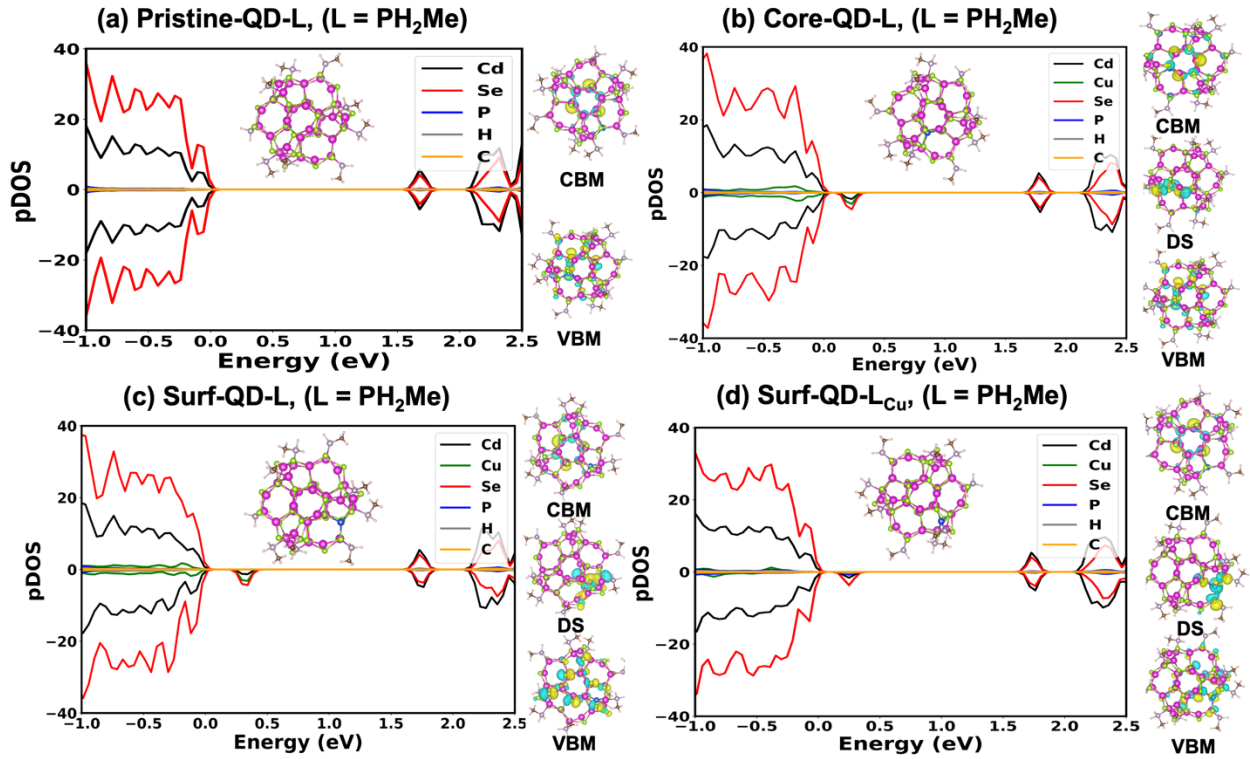


Figure S9: Optimized structures (in inset), the partial density of states (pDOS), and charge density (on the right panel) of (a) core-QD (core-QD-L), (b) surf-QD with unpassivated Cu-site (surf-QD-L), and (c) surf-QD with passivated Cu (surf-QD-$L_{Cu}$) where L=$PH_2Me$.

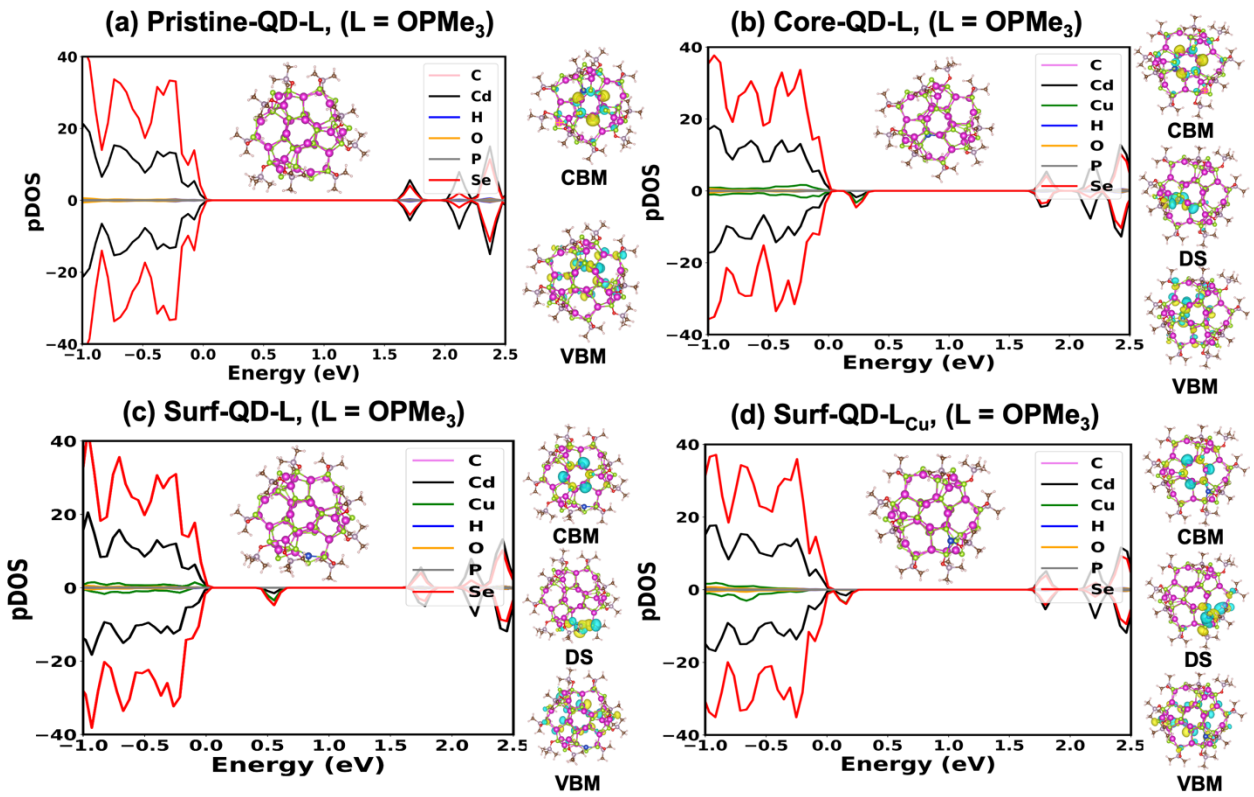


Figure S10: Optimized structures (in inset), the partial density of states (pDOS), and charge density (on the right panel) of (a) core-QD (core-QD-L), (b) surf-QD with unpassivated Cu-site (surf-QD-L), and (c) surf-QD with passivated Cu (surf-QD-$L_{Cu}$) where L=$OPMe_3$.

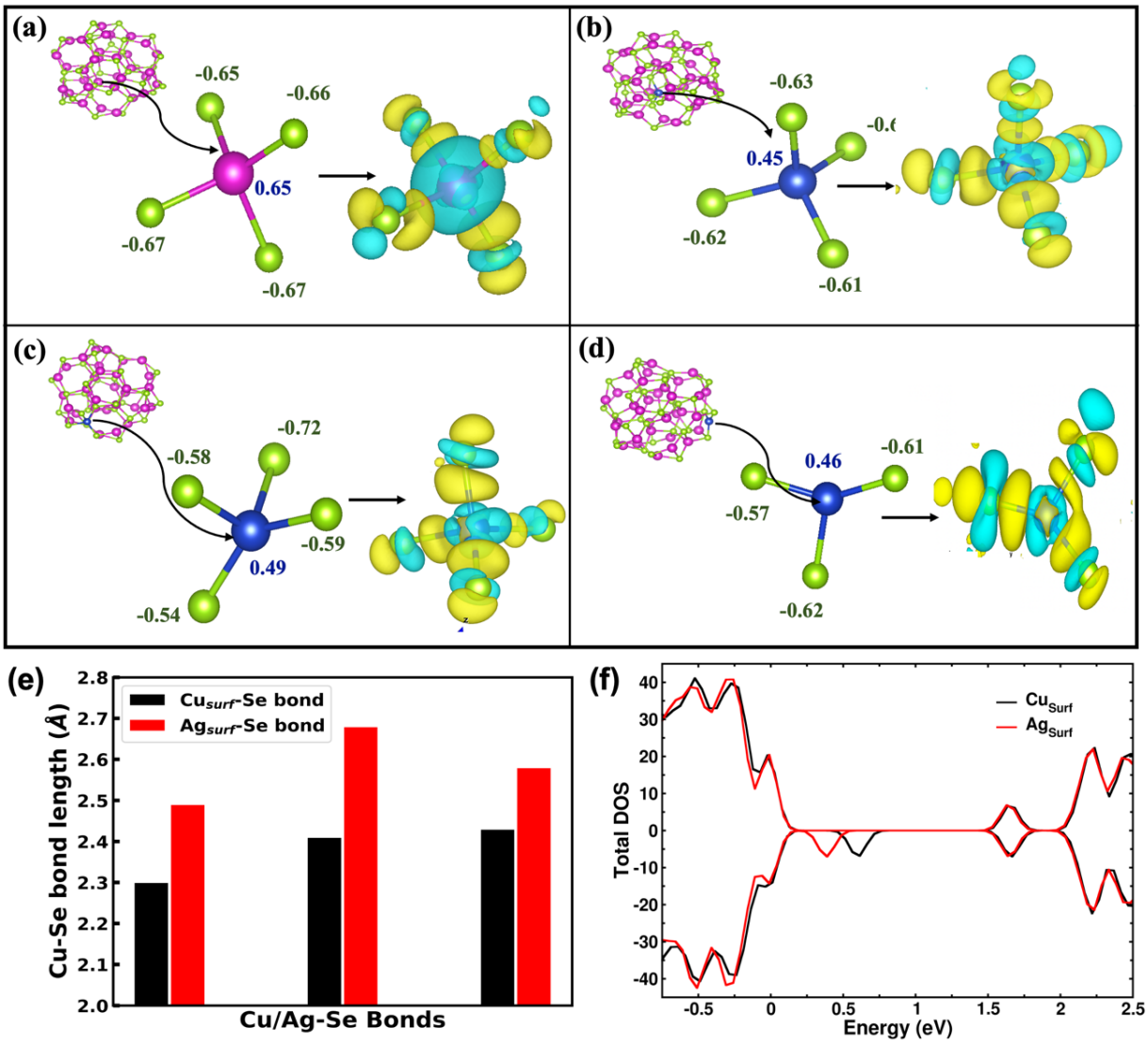


**Figure S11.** Investigation of the structure, Bader charge, and charge density difference for (a) Pristine $Cd_{33}Se_{33}$, (b) core-QD, (c) sub-QD, and (d) surf-QDs. (i) Structure: Visual representation of the atomic structure for each quantum dot configuration. (ii) Bader charge, the lesser positive charge of Cu (+0.68 $e^-$) compared to Cd indicates the more covalent and less polar nature of Cu-Se bonds than Cd-Se bonds. This observation also signifies a relatively higher charge transfer between Cd and Se in $Cd_{33}Se_{33}$. (iii) Charge density difference: Visualization of the difference in charge density distribution between the doped quantum dot configurations and pristine $Cd_{33}Se_{33}$. (e) $Cu_{surface}$-Se and $Ag_{surface}$-Se bond lengths. Surface Cu atoms are replaced with Ag, which has a

larger ionic radius. The relaxed geometry reveals that Ag-Se bonds are longer than Cu-Se bonds. (f) The total density of states (Total DOS) for $Cu_{surface}$-Se and $Ag_{surface}$-Se. The increased bond length between dopant and Se atoms subsequently shifts the defect state closer to the valence band maximum (VBM), with an energy difference of 0.38 eV above the VBM.

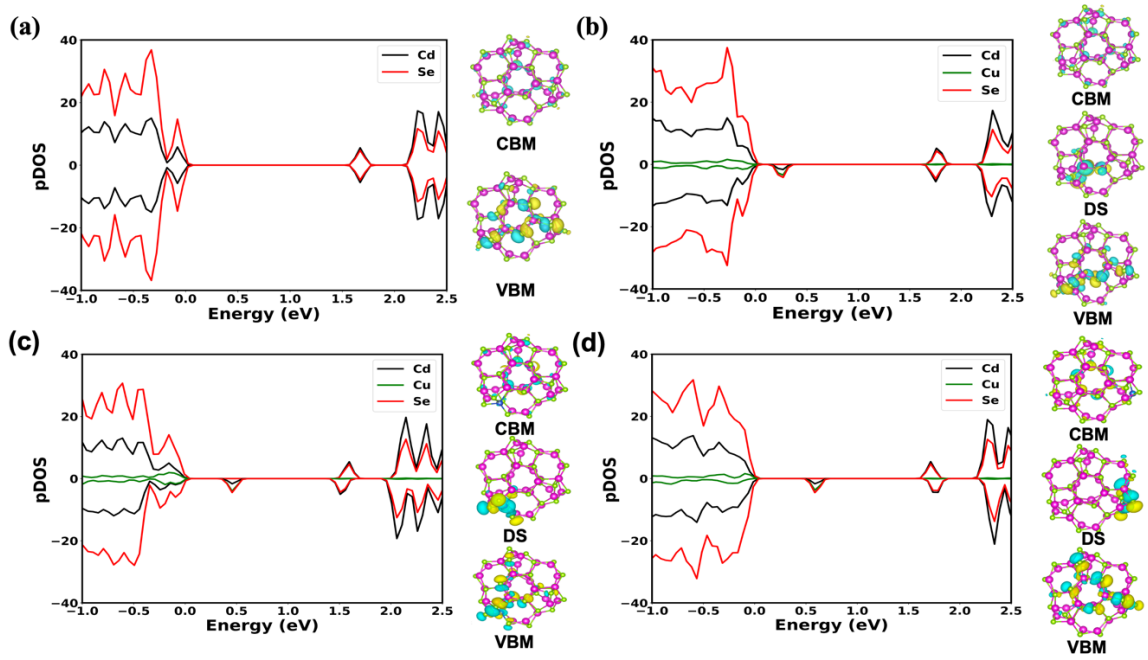


**Figure S12.** The projected density of states (pDOS) plots and the corresponding charge density distributions for the valence band maximum (VBM), defect state (DS), and conduction band minimum (CBM) in $Cd_{33}Se_{33}$ and doped quantum dots in the presence of water as a solvent for (a) Pristine $Cd_{33}Se_{33}$, (b) core-QD, (c) sub-QD, and (d) surf-QDs.

## S5. Computational Methodology

The pristine $Cd_{33}Se_{33}$ QD structure employed in this work has been derived from our previous work on investigating structural and electronic properties of semiconductor QDs, where the structures were optimized to their ground states.[1] Here, we utilized density functional theory (DFT) calculations and ab initio molecular dynamics (AIMD) simulations using the CP2K simulation package with the mixture of Gaussian and plane wave (GPW) basis set to run the static and

dynamical simulations of the QDs. [8,9] To approximate the exchange-correlation interactions in our calculations, we employed the generalized gradient approximation (GGA) with the Perdew-Burke-Ernzerhof (PBE) functional. The pristine and doped QD geometries were relaxed until the interatomic forces became less than 0.01 eV/ Å. In CP2K, the value of CUTOFF (the plane-wave cutoff in Ry) and REL_CUTOFF (the plane-wave cutoff of a reference grid covered by a Gaussian with a unit standard deviation $e^{|\bar{r}|^2}$) of 350 Ry and 50 Ry was taken.

The QDs were placed in a 30Å×30Å×30Å simulation cell, such that the periodic images were separated by at least 17 Å and did not have any spurious interactions. The formation enthalpy ($H_{form}$) was calculated using the equation $H_{form.} = [(E_{undoped}) - (E_{doped} + E_{Cu} - E_{Cd})$. Here, $E_{undoped}$ and $E_{doped}$ represent the total energies of the undoped $Cd_{33}Se_{33}$ and Cu-doped QDs, respectively, while $E_{Cd}$ and $E_{Cu}$ were the energies of a single atom of Cd and Cu placed in a vacuum. The static electronic properties were evaluated by plotting the partial density of states (pDOS), one-orbital Kohn-Sham (K-S) charge density distribution plot, and inverse participation ratio (IPR). The nature of the trap-states and charge distribution was further analyzed using Bader charge and charge density difference, respectively. [10,11] The charge density difference ($\Delta\rho$) for a Cu-doped $Cd_{33}Se_{33}$ QD, with Cu positioned at 'X' in the simulation box (where X is the position in core, subsurface, or surface), was calculated using the following equation: $\Delta\rho = \rho_{(Cd32CuSe33 \text{ with Cu at the position X})} - \rho_{(Cd32Se33 \text{ pristine QD})} - \rho_{(\text{only one Cu atom at X})}$.[12] Here, $\rho$ denotes the single-orbital K-S charge density of the system. The resulting $\Delta\rho$ signifies the charge density difference between the doped and undoped systems at the specified position. To calculate the migration barrier, the minimum energy path (MEP) is determined by the climbing-image nudged elastic band (CI-NEB) approach. The total potential energy convergence criterion is $1x10^{-6}$ eV. The force convergence at 0.015 eV.

Using eight intermediary images between the endpoints, a linear interpolation technique is used to create the initial approximate minimal energy path (MEP).

For quantifying the influence of thermal effects on the structure of the QDs, pair correlation function g(r), root mean square displacement (RMSD), root mean square fluctuation (RMSF), reorientation dynamics (rdyn), and histogram of bond length fluctuation were calculated. The RMSF is evaluated by measuring how much each atom fluctuated from its mean position during the MD production simulation. This provides an average fluctuation for each atom over the simulation, and the root mean square is evaluated considering all atoms of the same kind (Cd or Se). This calculation involves aligning the coordinates of all the atoms so that only the fluctuations of atoms can be measured, excluding the effects of translation and rotation of QD. This alignment and RMSF calculations were performed in the visual molecular dynamics (VMD) software. The power spectra were obtained from the AIMD trajectory by calculating the Fourier transform of the velocity autocorrelation function of the QD atoms. An open-access code, Trajectory Analyzer and Visualizer (TRAVIS) was utilized to obtain these power spectra. The Kohn-Sham electronic states were visualized using the VESTA v3.5.7 software package. The electronic structures of QDs at random timesteps were calculated using VASP. The plane-wave cutoff of 420 eV and the projected augmented wave method are employed. We use the wavefunctions further to calculate the inverse participation ratio (IPR). For evaluating IPR at random instant times, as discussed in the main text, we consider time t = 0.346, 1.73, 2.438, 3.475, 4.17, 5.525, 6.23, 7.592 ps for core and t = 0.445, 1.77, 2.12, 3.665, 4.17, 5.74, 6.413, 7.60 ps.

**S6. Root-Mean Square Fluctuations (RMSF)**

The RMSF measures how far a particle deviates from its reference position on average. It can gauge the structure's conformational stability throughout the simulation. Cu fluctuates more when

present in the core than on the surface, according to the RMSF plot in Figure 3a. To explore deeper into this discovery, the RMSF of each atom in the QD's surface and core was calculated, and the results are given in Figure S14b. The findings showed that surface atoms show more noticeable variations than core atoms. Geometrical fluctuations anticipate this result. We also looked into whether the Cu position affects the RMSF of atoms in the core and the surface and the overall dynamical properties of the QDs. Our findings show that the presence of Cu, regardless of where it is located, causes the atoms to fluctuate more. The confinement potential of electrons is further perturbed by the Cu atom, resulting in a broader distribution of the electron wavefunction. Additionally, the RMSF of every atom in core-QD and the Cu atom is somewhat higher than in surf-QD. The Cu atom's directional movement in the core is responsible for this observation. $Cu_{core}$ prefers to move towards the surface by rupturing the bond with one Se atom when exposed to thermal energy because the Cu atom is more stable there. This causes $Cu_{core}$ to become three-coordinated and move towards the surface. As a result of this transition, the ligand field's symmetry shifts from tetrahedral to planer trigonal, resulting in the fluxional behavior depicted in Figure 3b.

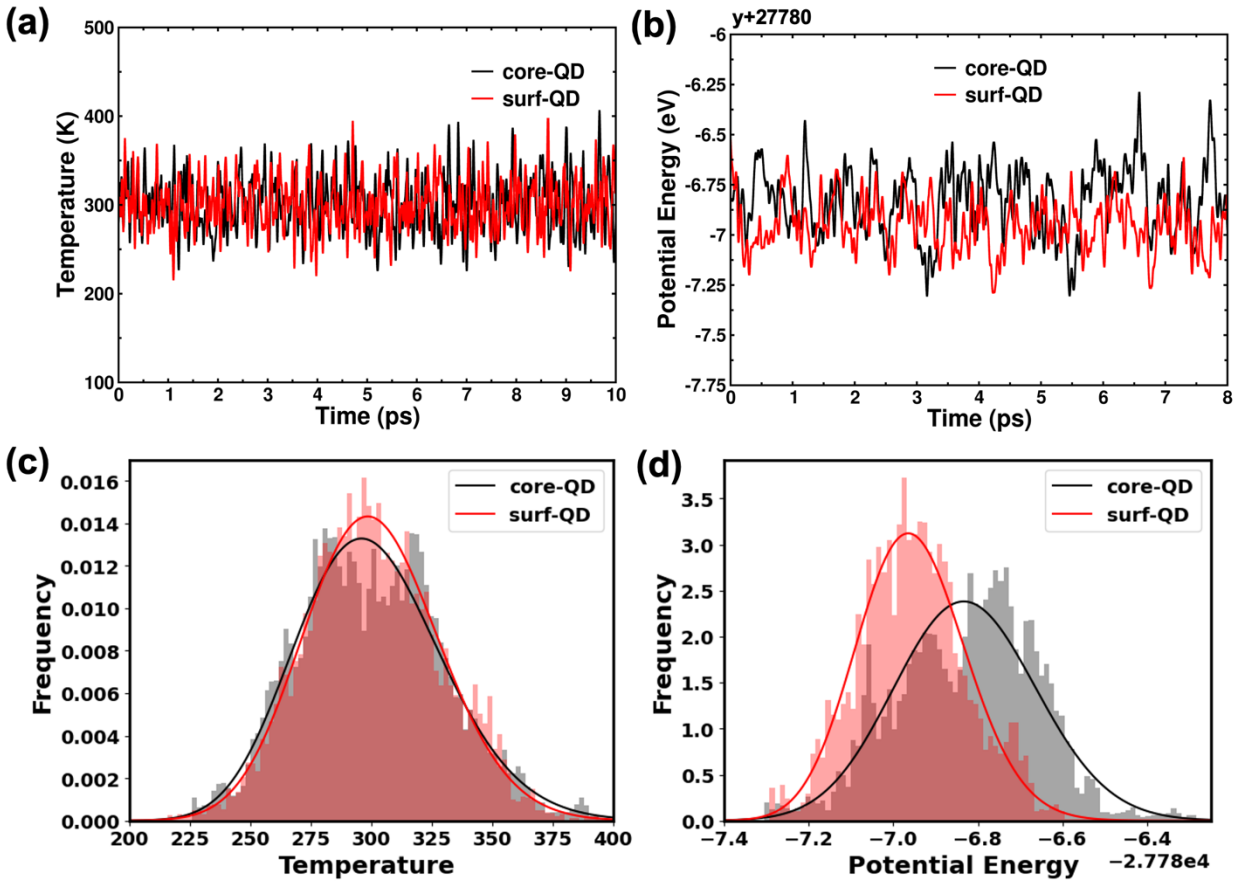


**Figure S13.** (a) Time vs. Temperature plot and (b) Potential energy curve demonstrating equilibration at 300K for conducting AIMD simulations. The histogram plots of (c) time vs. temperature and (d) potential energy vs. time.

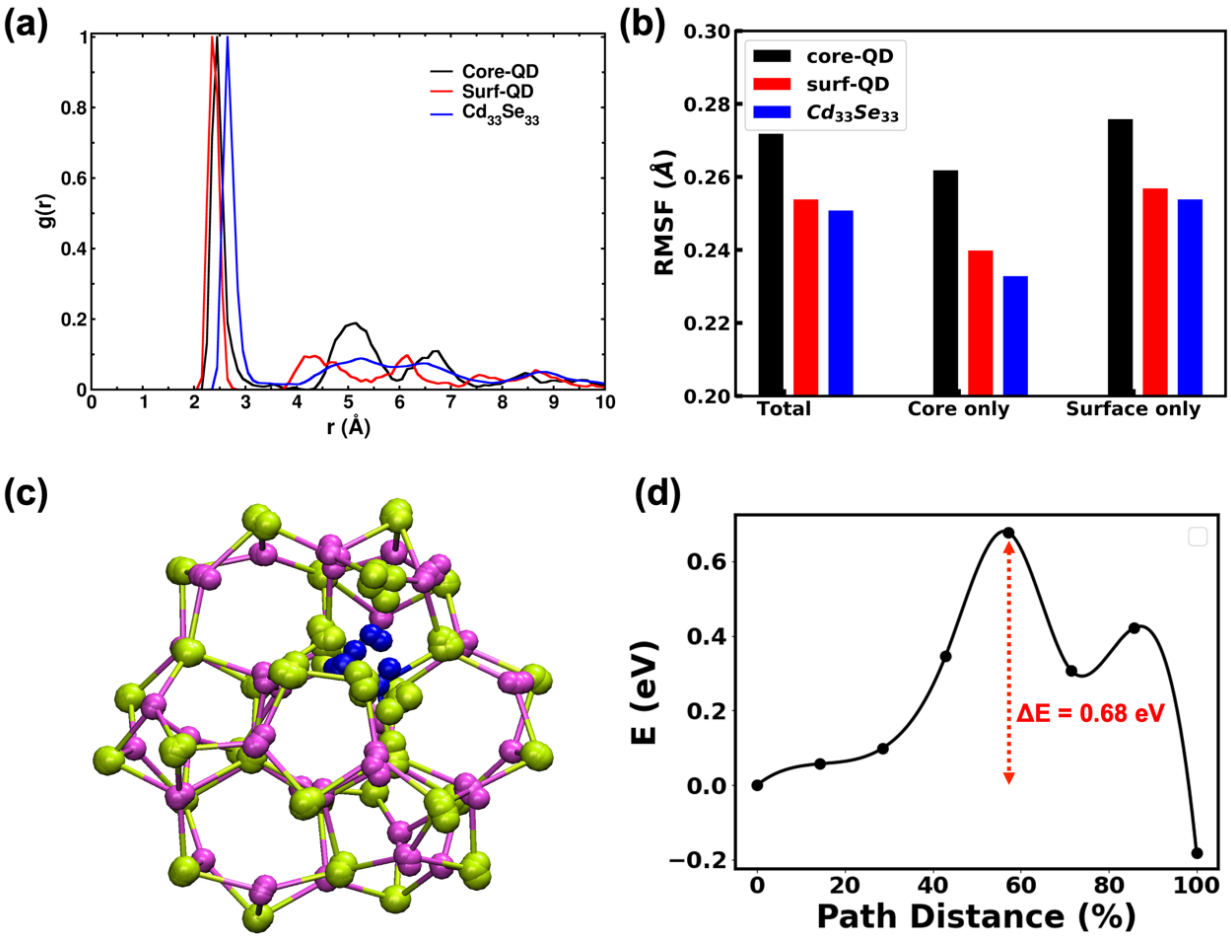


**Figure S14.** (a) Pair distribution functions g(r) illustrate the narrow distribution of bond distances (within 2-3 Å) for Cd-Se and Cu-Se bonds, confirming the stable geometric structures of the QDs. (b) Root-mean-square fluctuations (RMSF) quantify the thermal fluctuations of groups of atoms in the core and surface region of QD. The evaluated RMSFs reveal that surface atoms experience more significant thermal fluctuations than core atoms. (c) DFT-calculated Cu ion migration pathway using NEB, revealing significant local geometry distortion during copper diffusion, and (d) The energy barriers for vacancy-assisted Cu migration from subsurface to surface.

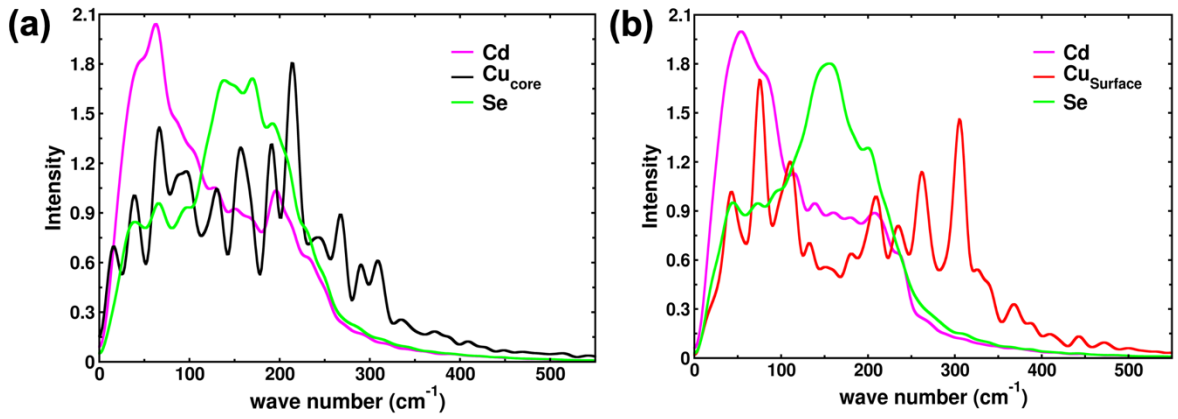


Figure S15: Vibrational density of states (vDOS) plot for the (a) core-QD and (b) surf-QD providing information on the vibrational modes and frequencies associated with these quantum dot configurations.

**S7. Band Gap Distribution**

The band edges that are VBM and CBM for the majority spin are included in Figure S17a,b. The distribution of the band gap is the gap between CBM and VBM, shown in Figure S17 for (c) majority spin and (d) minority spin. These energy distributions reveal that the thermal fluctuations affecting the bandgap and band edge states depend on the position of the dopant atom. The pristine $Cd_{33}Se_{33}$ QDs exhibit the broadest distribution of VBM (standard deviation of 0.081) and the narrowest distribution of CBM (standard deviation of 0.052). Additionally, Cu doping decreases the distribution of the VBM, while the distribution of CBM remains relatively unchanged. It is worth noting that the VBM level is more susceptible to thermal fluctuations of atoms compared to the CBM position in all of the studied QDs. Regarding surf-QDs, the standard deviations for VBM and CBM are 0.070 and 0.058, respectively. But, for core-QDs, the VBM and CBM levels are slightly shifted below and above, respectively, resulting in a high band gap and a slight blue shift. Moreover, the distribution of VBM and CBM in core-QD is slightly narrower, with standard deviations of 0.064 and 0.056, respectively. Although Cu doping leads to a decrease in the

distribution of VBM and an increase in the distribution of CBM, the extent of this change is relatively minor.

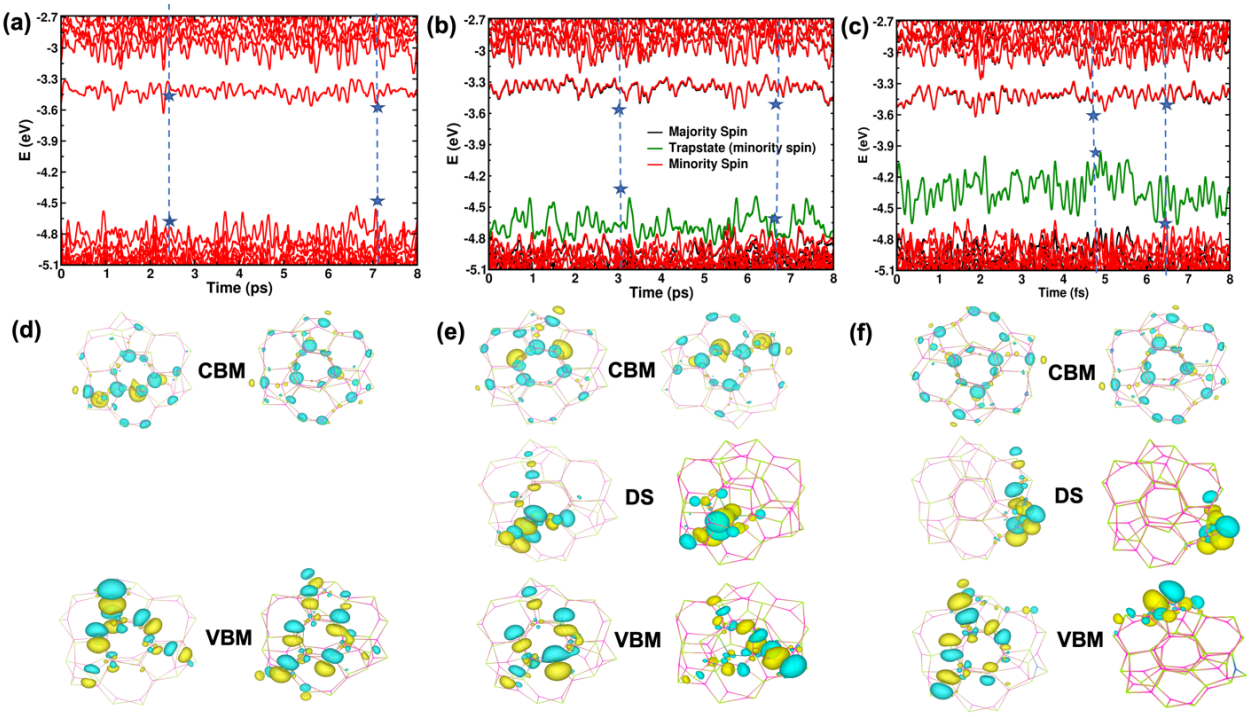


**Figure S16.** Energy state fluctuations with time for (a) $Cd_{33}Se_{33}$, (b) core-QD, and (c) surf-QD. The charge density of band edges and defect state orbitals at two specific time instants illustrate the maximum and minimum gaps between the VBM and CBM time for (d) $Cd_{33}Se_{33}$, (e) core-QD, and (f) surf-QD.

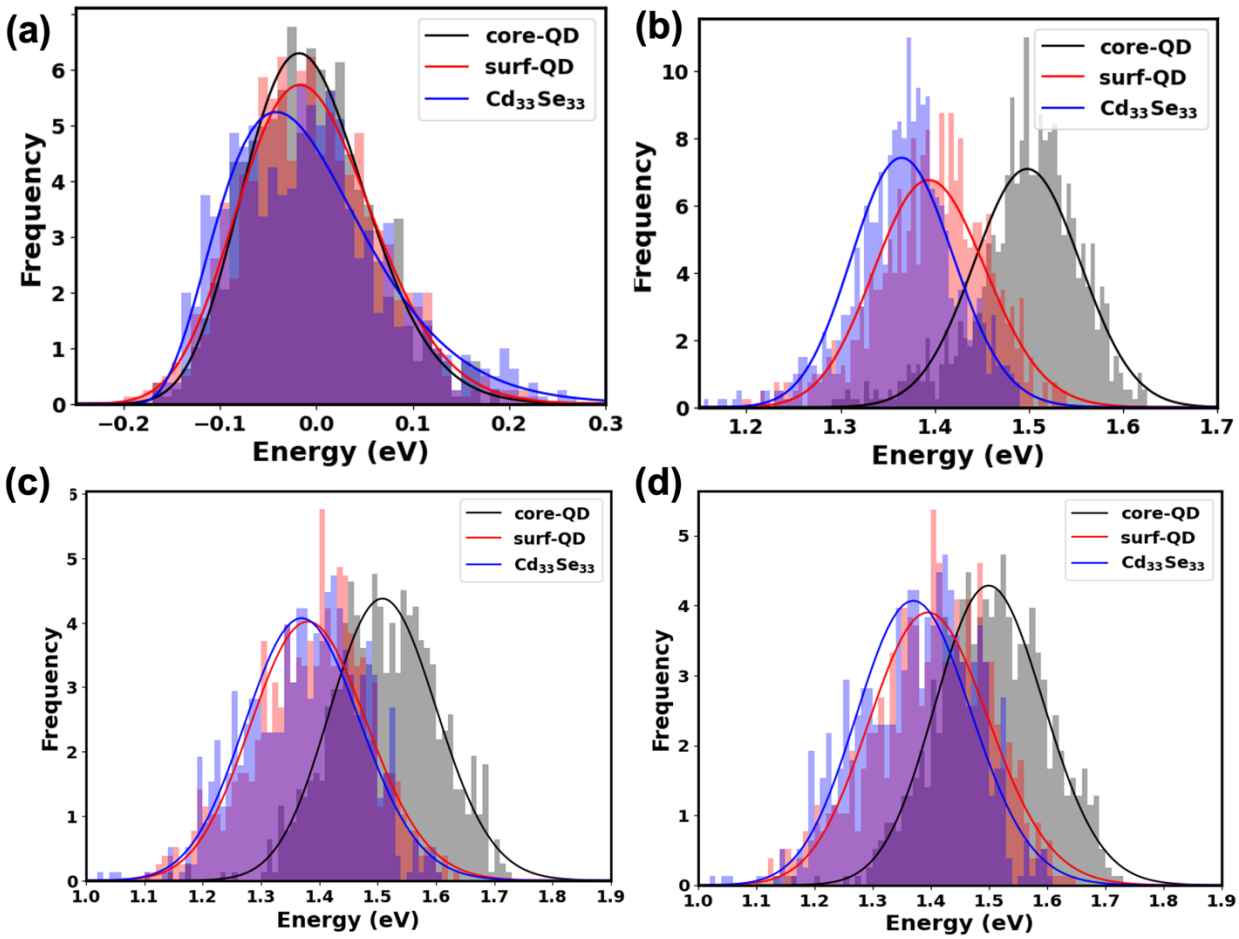


**Figure S17.** The (a) VBM and (b) CBM for minority spin in pristine $Cd_{33}Se_{33}$ and doped QDs. The distribution of the energy gap between CBM and VBM for (c) majority spin and (d) minority spin and band edges.

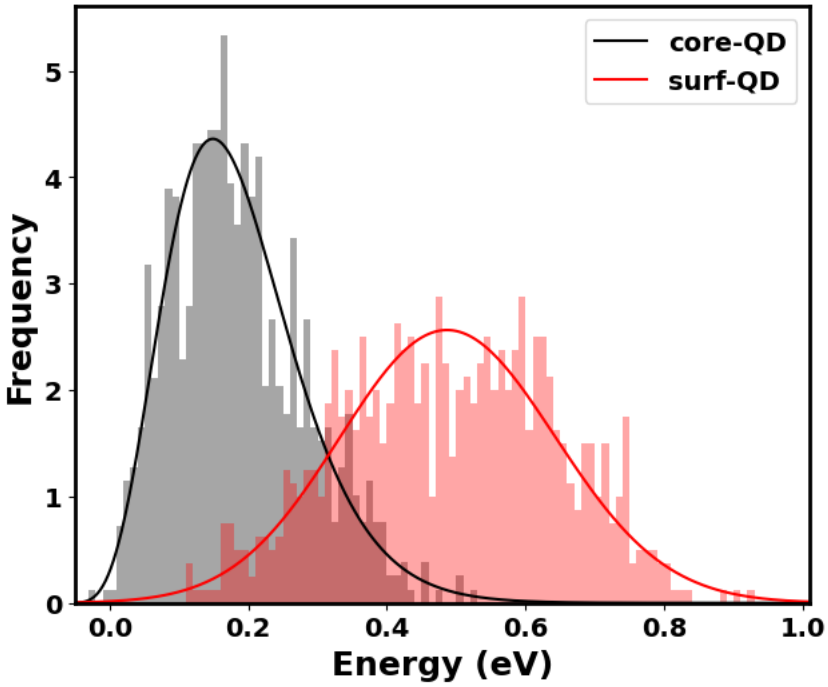


**Figure S18.** Histogram for fluctuation of the gap between VBM and defect state for core-QD and surf-QD

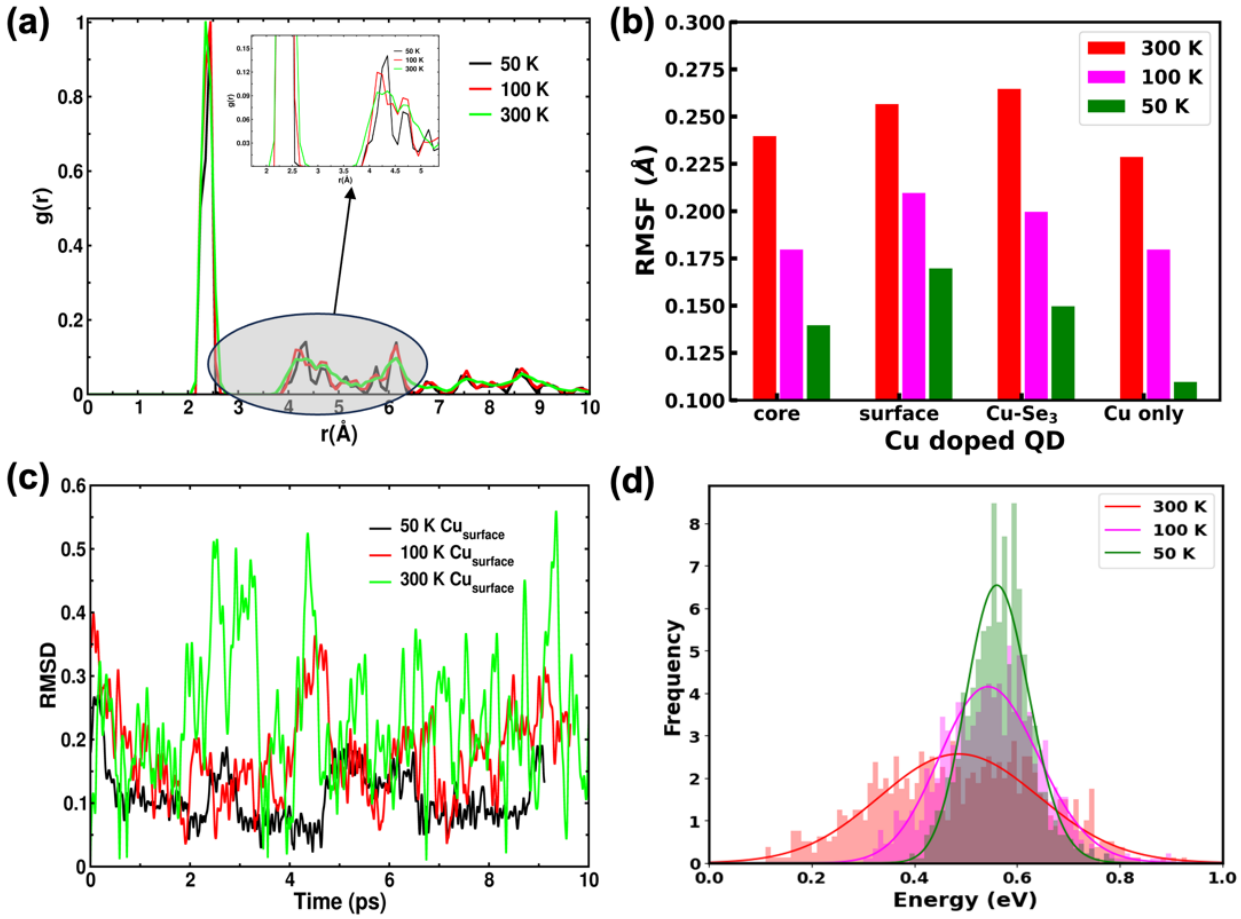


**Figure S19.** The photophysical properties of surf-QD are explored at low temperatures of 50 and 100 K. The plotted (a) pair distribution functions g(r) for Cd-Se and Cu-Se demonstrate that the distribution of bond distances narrows down as the temperature decreases. Furthermore, the reduction in (b) RMSD and (c) RMSF values, as included in confirm the suppressed structural fluctuations in surf-QD at low temperature, (d) demonstrates the histogram plot of mid-gap state positions at 50 K and 100 K for surf-QD. The distribution is much broader at 300 K (Figure 4c), while it becomes narrower as the temperature decreases. The standard deviations for defect state position are 0.051, 0.087, and 0.139 for 50, 100, and 300K, respectively.

## REFERENCE:


(1) Ghosh, D.; Ivanov, S. A.; Tretiak, S. Structural Dynamics and Electronic Properties of Semiconductor Quantum Dots: Computational Insights. *Chemistry of Materials* **2021**, *33* (19), 7848–7857. https://doi.org/10.1021/acs.chemmater.1c02514.

(2) Kilina, S.; Ivanov, S.; Tretiak, S. Effect of Surface Ligands on Optical and Electronic Spectra of Semiconductor Nanoclusters. *J Am Chem Soc* **2009**, *131* (22), 7717–7726. https://doi.org/10.1021/ja9005749.

(3) Jain, A.; Ong, S. P.; Hautier, G.; Chen, W.; Richards, W. D.; Dacek, S.; Cholia, S.; Gunter, D.; Skinner, D.; Ceder, G.; Persson, K. A. Commentary: The Materials Project: A Materials Genome Approach to Accelerating Materials Innovation. *APL Materials*. American Institute of Physics Inc. 2013. https://doi.org/10.1063/1.4812323.

(4) Fischer, S. A.; Crotty, A. M.; Kilina, S. V.; Ivanov, S. A.; Tretiak, S. Passivating Ligand and Solvent Contributions to the Electronic Properties of Semiconductor Nanocrystals. *Nanoscale* **2012**, *4* (3), 904–914. https://doi.org/10.1039/c2nr11398h.

(5) Kirkwood, N.; Monchen, J. O. V.; Crisp, R. W.; Grimaldi, G.; Bergstein, H. A. C.; Du Fossé, I.; Van Der Stam, W.; Infante, I.; Houtepen, A. J. Finding and Fixing Traps in II-VI and III-V Colloidal Quantum Dots: The Importance of Z-Type Ligand Passivation. *J Am Chem Soc* **2018**, *140* (46), 15712–15723. https://doi.org/10.1021/jacs.8b07783.

(6) Liu, I. S.; Lo, H. H.; Chien, C. T.; Lin, Y. Y.; Chen, C. W.; Chen, Y. F.; Su, W. F.; Liou, S. C. Enhancing Photoluminescence Quenching and Photoelectric Properties of CdSe Quantum Dots with Hole Accepting Ligands. *J Mater Chem* **2008**, *18* (6), 675–682. https://doi.org/10.1039/b715253a.

(7) Anderson, N. C.; Hendricks, M. P.; Choi, J. J.; Owen, J. S. Ligand Exchange and the Stoichiometry of Metal Chalcogenide Nanocrystals: Spectroscopic Observation of Facile

Metal-Carboxylate Displacement and Binding. *J Am Chem Soc* **2013**, *135* (49), 18536–18548. https://doi.org/10.1021/ja4086758.

(8) Kühne, T. D.; Iannuzzi, M.; Del Ben, M.; Rybkin, V. V.; Seewald, P.; Stein, F.; Laino, T.; Khaliullin, R. Z.; Schütt, O.; Schiffmann, F.; Golze, D.; Wilhelm, J.; Chulkov, S.; Bani-Hashemian, M. H.; Weber, V.; Borštnik, U.; Taillefumier, M.; Jakobovits, A. S.; Lazzaro, A.; Pabst, H.; Müller, T.; Schade, R.; Guidon, M.; Andermatt, S.; Holmberg, N.; Schenter, G. K.; Hehn, A.; Bussy, A.; Belleflamme, F.; Tabacchi, G.; Glöß, A.; Lass, M.; Bethune, I.; Mundy, C. J.; Plessl, C.; Watkins, M.; VandeVondele, J.; Krack, M.; Hutter, J. CP2K: An Electronic Structure and Molecular Dynamics Software Package -Quickstep: Efficient and Accurate Electronic Structure Calculations. *Journal of Chemical Physics*. American Institute of Physics Inc. May 21, 2020. https://doi.org/10.1063/5.0007045.

(9) Kresse, G.; Hafner, J. *Ab. Initio Molecular Dynamics for Liquid Metals*; Vol. 47.

(10) Yu, M.; Trinkle, D. R. Accurate and Efficient Algorithm for Bader Charge Integration. *Journal of Chemical Physics* **2011**, *134* (6). https://doi.org/10.1063/1.3553716.

(11) Henkelman, G.; Arnaldsson, A.; Jónsson, H. A Fast and Robust Algorithm for Bader Decomposition of Charge Density. *Comput Mater Sci* **2006**, *36* (3), 354–360. https://doi.org/10.1016/j.commatsci.2005.04.010.

(12) Tozini, D.; Forti, M.; Gargano, P.; Alonso, P. R.; Rubiolo, G. H. Charge Difference Calculation in Fe/Fe3O4 Interfaces from DFT Results. *Procedia Materials Science* **2015**, *9*, 612–618. https://doi.org/10.1016/j.mspro.2015.05.037.